Open access • Journal Article • DOI:10.1109/TIE.2013.2281152

A Hybrid-Excited Flux-Switching Machine for High-Speed DC-Alternator Applications — Source link

Benjamin Gaussens, Emmanuel Hoang, Michel Lecrivain, Philippe Manfe ...+1 more authors

Published on: 01 Jun 2014 - IEEE Transactions on Industrial Electronics (IEEE)

Topics: Stator, Rotor (electric), Topology (electrical circuits), Electromagnetic coil and Alternator (automotive)

An Hybrid-Excited Flux-Switching Machine for High Speed DC-Alternator Applications

Benjamin Gaussens, Emmanuel Hoang, P. Manfe, Michel Lécrivain, Mohamed Gabsi

An Hybrid-Excited Flux-Switching Machine for High Speed DC-Alternator Applications

Benjamin Gaussens, *Student Member, IEEE*, Emmanuel Hoang, Michel Lécrivain, Philippe Manfe, and Mohamed Gabsi

***Abstract*—This paper presents a new topology of Hybrid Excited Flux-Switching Machine (HE FSM) with excitation coils located in stator slots (or inner DC windings). After describing the three phase structure to be investigated, the working principle is discussed and main electromagnetic performances are simulated by Finite Element (FE) Analysis. It is demonstrated that the air-gap field can be easily controlled which is interesting for variable-speed applications. Finally, a prototype having 12 stator poles and different rotor teeth number (10 or 14) was built. Experiments were performed validating FE simulations and the operation principle. Finally, the thermal behavior of the prototype machine is investigated through experiments. It is shown that up to 12000rpm, the thermal stabilization is achieved, making this topology an excellent candidate for high-speed applications.**

***Index Terms*—Brushless machine, finite element analysis, hybrid excited, flux-switching.**

I. Introduction

THE flux-adjusting capability of permanent magnet (PM) machines was extensively studied in the past [1]. Flux weakening operation allows PM motors to operate over the base speed by injection of negative d-axis current[2]. However, partial demagnetization of PM is likely to happen. Thus, an alternative solution for flux control is to modify the electromagnetic design by introducing an additional wound exciter.

In the literature, many hybrid excited topologies can be found [3], most of them derived from claw-pole [4], consequent pole [5], doubly salient [6] or flux-switching [7][8] machines.

Hybrid excited flux-switching machines (HE-FSM) are excellent candidates for wide speed constant power operation thanks to their high torque density and high speed capability (with a robust passive rotor). Also, they inherit the good fault-tolerant ability of alternate PM-excited Flux-Switching machines[9][10][11][12]. From literature, different HE-FSM can be listed and classified as series flux-path HE-FSM [13] or as parallels flux-path HE-FSM [14][15][16].

Manuscript received January 31, 2013. Accepted for publication August 4, 2013.

M. Gaussens, M. Hoang, M. Lecrivain and M. Gabsi are with the SATIE laboratory, ENS Cachan, CNRS, UniverSud, 61 av. du President Wilson, Cachan F-94230, France (e-mail : gaussens@satie.ens-cachan.fr, hoang@satie.ens-cachan.fr, ecrivain@satie.ens-cachan.fr and gabsi@satie.ens-cachan.fr).

M. Manfe is with Leroy Somer, Emerson, EPG Division, Sillac, Bd Marcellin Leroy - 16015 Angoulême Cedex, France (e-mail : philippe.manfe@emerson.com).

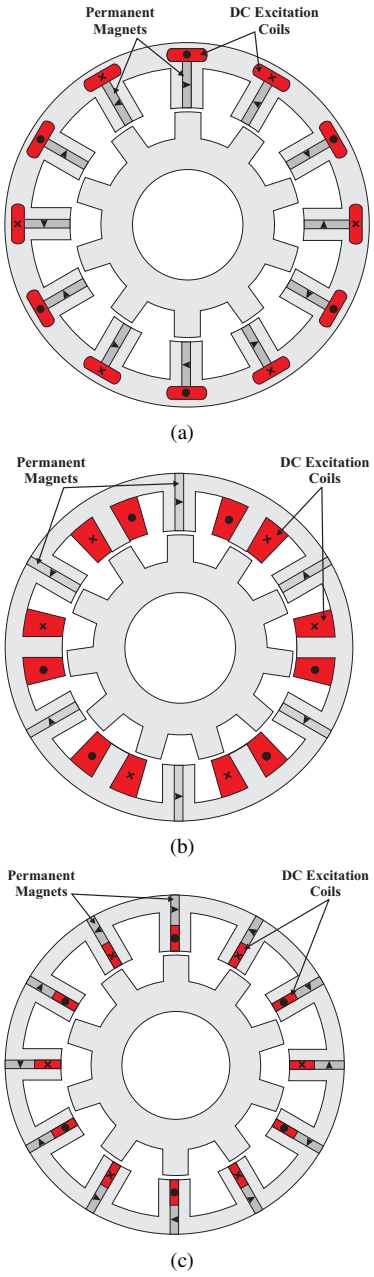

Fig. 1. Existing topologies of Hybrid-Excited Flux-Switching Machines : Hoang *et al.* [14] (a), Chen *et al.* [15] (b) and Hua *et al.* [13] (c)

The high speed operation of Permanent Magnet machine is severely strained by mechanical and thermal limitations. Regarding mechanical stress, the hybrid-excited flux-switching

machine that is explored, can rotate easily at high speeds because all the active parts are housed in the stator [17]. Regarding the thermal behavior, we demonstrate in this work the suitability of this topology through experiments.

The paper is organized as follows. In Section II, an analysis of working principle of existing HE-FS machine is proposed. The proposed topology is introduced in Section III. Then, the operation principle is carried out based on FE Analysis. In the fourth section, the influence of hybridization on the machine design is acknowledged. Then, in Section V, we will discuss to which group, series or parallels flux-path HE-FSM, this new topology belongs. In Section VI, a prototype was built to confirm the field-regulation capability of this structure. Finally, we investigated the thermal behavior of the prototype machine under high speeds (up to 12000rpm) and in flux-weakening mode.

II. Analysis of existing HE-FS Machines

To emphasize the innovation of the proposed HE-FS topology (See Section III), we propose in this section an analysis of existing HE-FS structures, presented in Fig. 1. The working principle of those three topologies just requires to focus on an elementary cell. Flux lines created by permanent magnet (PM) are depicted on Fig. 2 for each existing topology. The DC coils are not powered.

As can be seen, in Fig. 2.(a), the PM flux is short-circuited magnetically. On the contrary, for topologies presented in Figs .2.(b) and (c), the PM flux links through the rotor. That means that without DC excitation current, the flux-linkage should be higher.

In Fig. 3, evolution of flux-linkage as function of DC excitation magnetomotive force NI_{exc} is proposed, for the three topologies. As shown, topologies 2 and 3 do not exhibit a high flux-linkage control capability in comparison with topology 1. However, topology 2 has a higher flux-linkage because of a high flux focusing effect (See Fig. 2.(b)). Nevertheless, as explained in [15], this topology is working with an odd number of rotor teeth. That may induce unbalanced magnetic forces and thus create undesired magnetic vibrations.

In next sections, a novel hybrid-excited flux switching machines is proposed. Its unconventionnal working principle was particularly studied.

III. Proposed HEFS Topology

Fig. 4 shows a cross section view of the proposed 12 slots - 10 poles HEFS Machine with inner DC winding. This structure is based on a conventional FSPM machine but with a DC winding located directly in the slot area which is usually dedicated to the armature winding.

In this paper, two stator configurations are considered: the first one with the DC excitation coils over the armature coils (Upper Located DC winding UL-DCw) and also the reverse situation, *i.e.* with the excitation winding situated near the air-gap (Lower Located DC winding LL-DCw), above the phase windings (respectively Figs. 5.(a) and (b)).

Each stator pole is fully wound with non-overlapping armature windings. Regarding the excitation winding, it could

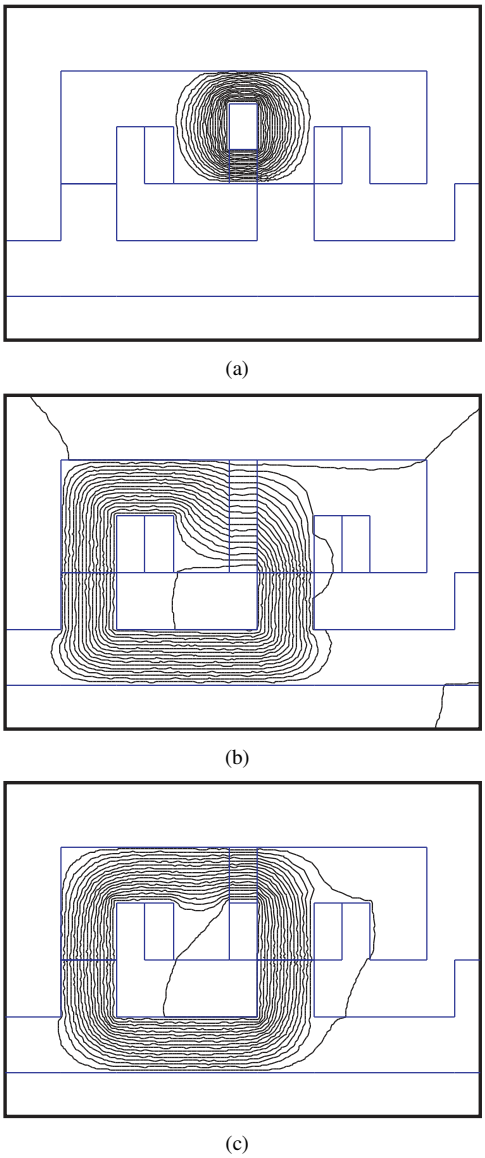

Fig. 2. Linearized elementary cell with only the permanent magnet (the DC coil is not powered): Hoang *et al.* [14] (a), Chen *et al.* [15] (b) and Hua *et al.* [13] (c)

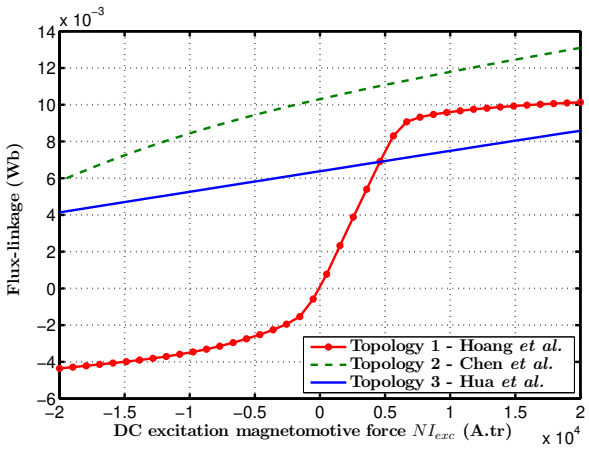

Fig. 3. Evolution of flux-linkage as function of magnetomotive force NI_{exc}

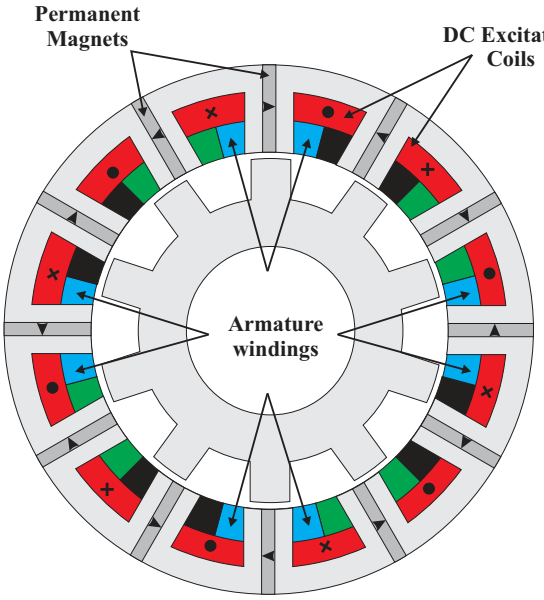

Fig. 4. Proposed Hybrid-Excited Flux-Switching Machine

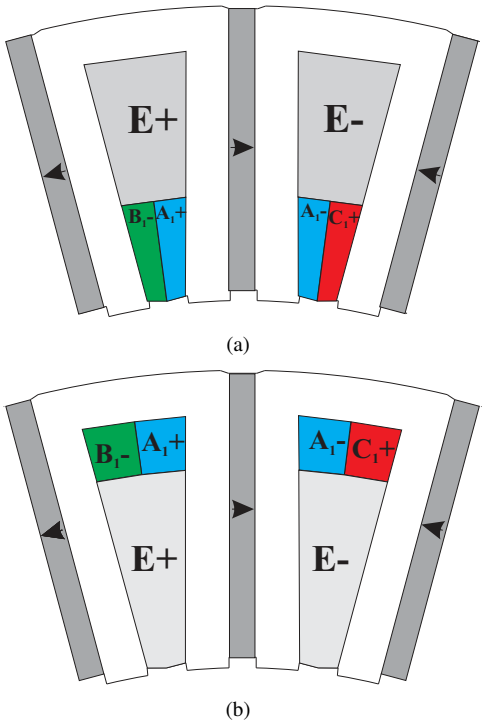

Fig. 5. Cross section of elementary cell: Upper Located DC winding (UL-DCw) Structure, (b) Lower Located DC winding (LL-DCw) Structure

be wound like a phase coil and then, connected in series while respecting the order E+ E-. It is worth mentioning that, unlike classical HEFSM [14][13], the maximum flux-linkage is set up by the PM field, thus only flux weakening could be achieved. We explore only double-layer configurations in this paper. Also, the outer diameter of the machine is inevitably increased due to the DC coils. Nonetheless, this topology offers a significant additional space in the radial direction, which can be filled by:

- Rare-earth permanent magnet for high torque density applications; or by
- Low-remanence material, like ferrite or bonded NdFeB magnet, for a low-cost application.

IV. Operation Principle

Similar to the classical FSPM machine, in the HEFSM with inner DC winding, the negative and positive maximum flux-linkage of coil A_1 occurs when a rotor pole is approximately aligned with one of the stator teeth (Figs. 6.(a) and (b)). Therefore, a movement of the rotor induce a bipolar flux-linkage and hence, an alternating back-emf. As mentioned in the literature [18], the flux-linkage seen by two-adjacent coils of the same phase are asymmetric, however the phase flux-linkage has a sinusoidal-like waveform.

In existing HEFS topologies, the focus on just one elementary cell is enough to understand the operating principle. Here, the influence of current injection in the DC winding has to be investigated considering two adjacent coils (A_1 and A_2). Fig. 6 illustrates the action of DC winding on each coil, respectively for the minimum and the maximum flux-linkage. On this extended view of the magnetic circuit of the UL-DCw structure, both sources flux lines are depicted, *i.e.* PM flux lines in green and DC winding flux lines in red dashed lines. Furthermore, this shematic operating diagram is complemented by individual (coils A_1 and A_2) and total phase flux-linkage waveforms with different DC excitation current density (Fig. 7).

Considering the rotor position of Fig. 6.(a), when the flux-linkage is minimum, the injection of DC current will introduce a positive homopolar component in coil A_1 (negative for coil A_2) enhancing the mean value of coil A_1 flux-linkage (and weakening the mean value of coil A_2 flux-linkage). Meanwhile, the PM flux of coil A_2 is smoothed over since the DC winding induces a field in opposite way of PM flux.

A $360/2.N_r$-degree mechanical rotation of the rotor leads to the configuration shown Fig. 6.(b), where the flux-linkage of phase A is maximum. Here, the flux-linkage of coil A_1 is spread out while the one of coil A_2 is straightening. Finally, as the DC current increases, the flux-linkage variation over an electric period decreases (See Fig. 8). Even though each coil flux-linkage waveform is distorted, the spectra of the sum $\varphi_{A_1} + \varphi_{A_2}$, *i.e.* of the phase flux-linkage, reveals a low-harmonic content,as shown in Figs. 7.(d), (e) and (f). Also, on spectras on Figs. 7.(d), (e) and (f), it can be noted that the homopolar component of each coil increases with the DC excitation current. However, the total flux-linkage does not exhibit any mean value.

In Fig. 9, the evolution of the peak phase flux-linkage as function of the DC field current density is proposed. As can be seen, a good flux-weakening is achieved for both configurations. The LL-DCw structure, due to proximity of air-gap, exhibits a greater efficiency of DC windings only for high DC excitation current density δ_{exc}. Also, in Fig. 9 is superimposed the evolution of the peak flux-linkage with or without iron bridges (only for the UL-DCw topology). Indeed, to ease manufacturing, U-shaped stator cores are linked with an iron bridge (IB)(See Fig. 19). As expected, the PM flux is

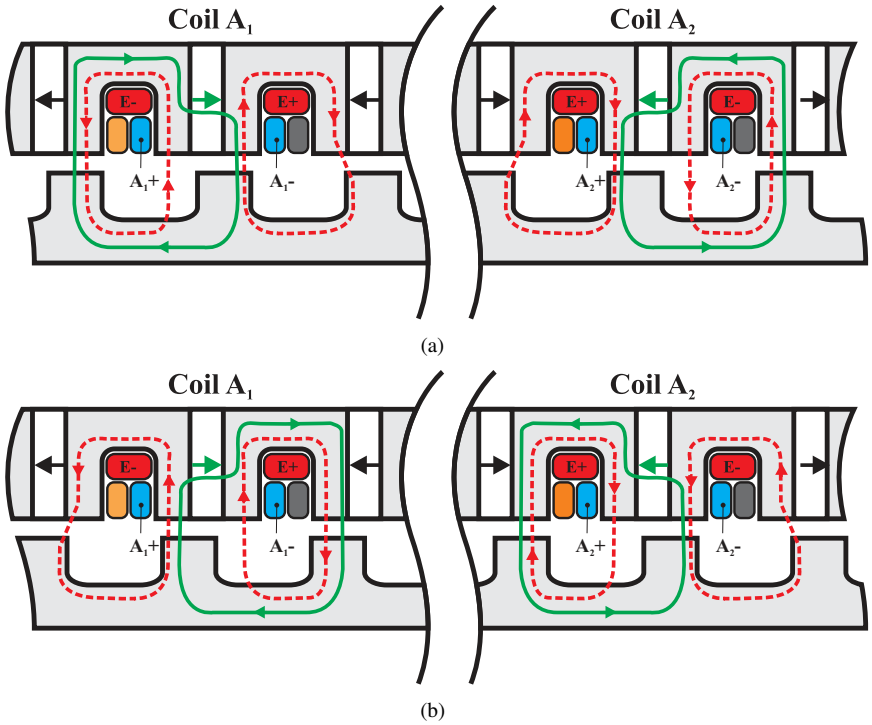

Fig. 6. The extended magnetic circuit of the UL-DCw Structure for the minimum (a) and maximum (b) flux-linkage of phase A : PM flux (green lines) and DC field winding flux (red dashed lines)

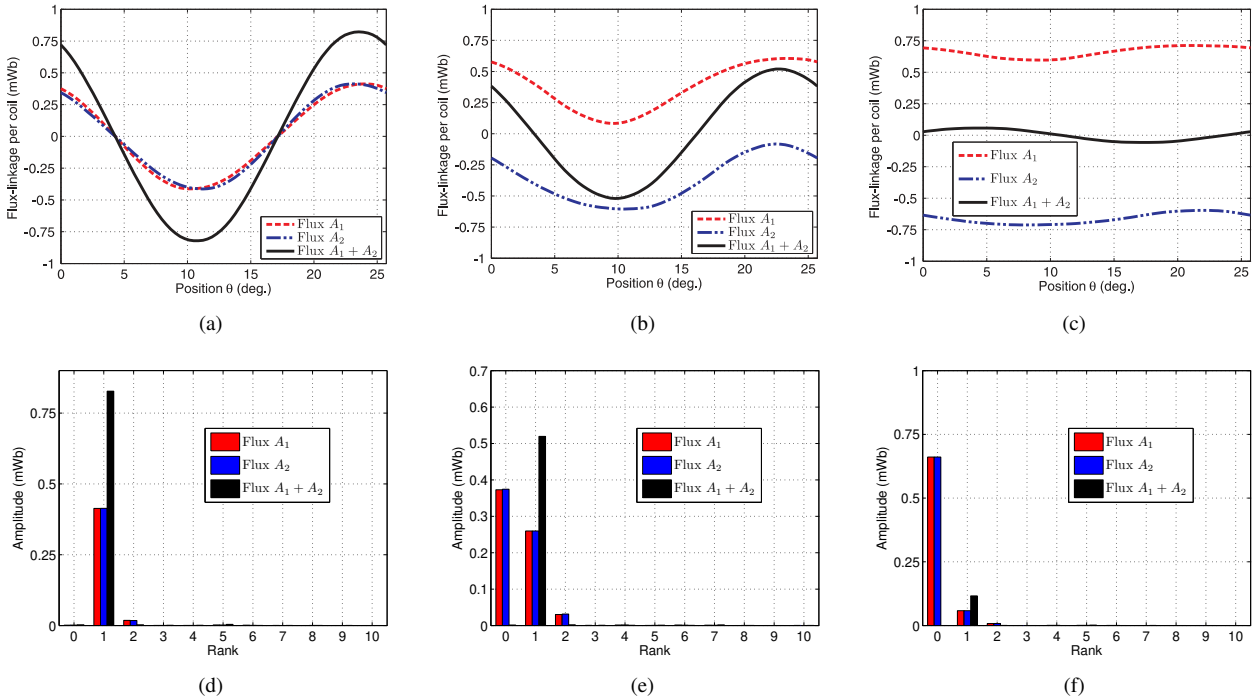

Fig. 7. Evolution of flux-linkage of two adjacent coils for the same phase A_1 and A_2 as function of position for different DC excitation current density: $\delta_{exc} = 0A.mm^{-2}$ (a), $\delta_{exc} = 5A.mm^{-2}$ (b), $\delta_{exc} = 10A.mm^{-2}$ (c) and their spectras (d)(e)(f) - UL-DCw structure with a 14-teeth rotor

directly short-circuited. The UL-DCw arrangement with iron bridge has a lower peak flux-linkage ($2-3\%$ with a 1mm iron bridge), which will result in a slightly lower torque capability.

We can also notice that the armature flux-linkage is shifted due to the injection of DC current (Fig. 8). This means that the $d-$axis of the structure is modified when the DC winding is powered. This effect is investigated in Fig. 10, where the evolution of the peak flux-linkage for $\theta_{max} = 23.5°C$ (mechanical angular position corresponding to the peak flux-linkage at $\delta_{exc} = 0A.mm^{-2}$) and for $\theta_{max}(\delta_{exc})$ are pictured. For both considered configurations, the introduced phase de-

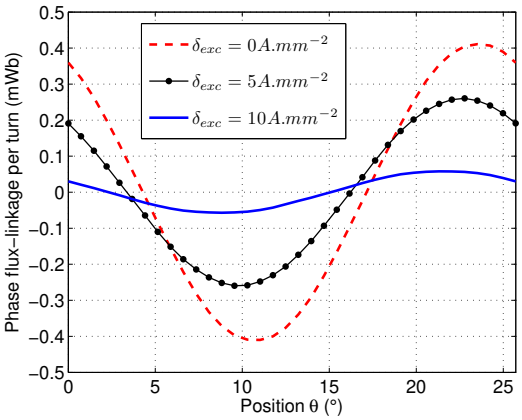

Fig. 8. Evolution of phase flux-linkage per turn as function of rotor position θ and for different DC excitation current density δ_{exc} - UL-DCw configuration with 14-teeth rotor

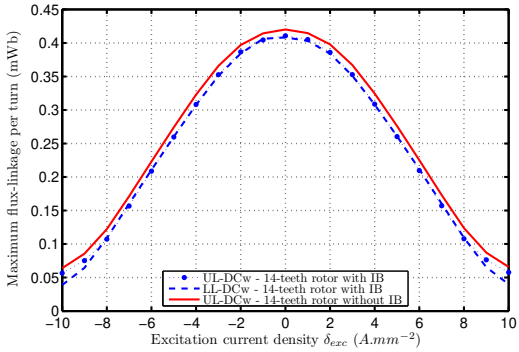

Fig. 9. Evolution of peak flux-linkage φ_{max} as function excitation current density δ_{exc} for UL-DCw and LL-DCw configurations with or without Iron Bridges (IB)

viation does not introduce a significant uncertainty about the peak value of flux-linkage.

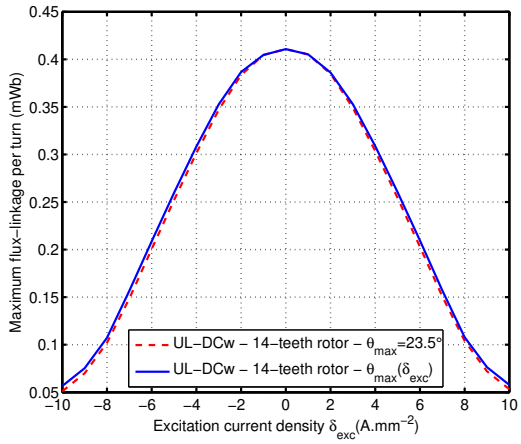

Fig. 10. Evolution of peak flux-linkage φ_{max} as function excitation current density δ_{exc} for UL-DCw topologie at $\theta_{max} = 23.5°C$ and $\theta_{max}(\delta_{exc})$

Last but not least, the location of DC winding directly on the PM flux path inevitably force each DC excitation coil to embrace an alternating flux. Although, the total flux-linkage of the DC excitation does not present high variation, as predicted in Fig. 11. Furthermore, it could be remarked that, as the DC excitation current density δ_{exc} rises, the total flux-linkage variation reduces. Hence the induced back-emf on the DC winding won't be significant to disturb the DC source. A special attention must be paid to this when sizing a prototype machine.

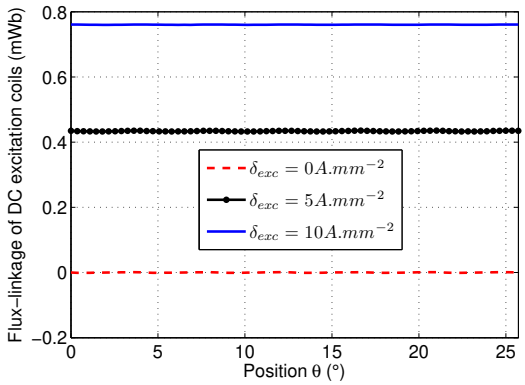

Fig. 11. Evolution of DC winding flux-linkage as function of postion θ for different DC excitation current density δ_{exc}

V. Influence of Hybridization on the Machine Design

The location of DC winding inside stator slot reduces the slot area dedicated to armature windings. Hence, the machine design should be definitely impacted. In this section, we acknowledge this influence using power equations.

The comparison is performed only with a classical Permanent Magnet Flux-Switching (PM-FS) machine. Indeed, both structures, PM-FS and HE-FS machines with inner DC windings, show a high degree of similarity regarding their topologies.

A. Maximum output power based on power equation approach

As explained before, to determine the maximum output power, we use a power equation approach. In Fig. 12, a cross section view of an elementary cell is proposed. This elementary cell we will be used to determine influence of the DC winding on electromagnetic performances.

The subscript PM refers to the PM-FS machine and subscript HE to the HE-FS machine with inner DC windings.

1) Classical PM Flux-Switching Machine

The maximum output power of a classical PM Flux-Switching machine $P_{max_{PM}}$ can be expressed as a function of two terms, $NI_{cc_{PM}}$ the short-circuit magnetomotive force and $\Phi_{exc_{PM}}$ the no-load flux-linkage,

$$P_{max_{PM}} \propto NI_{cc_{PM}}.\Phi_{exc_{PM}} \tag{1}$$

with

$$\Phi_{exc_{PM}} \propto B_r.h_{a_{PM}} \tag{2}$$

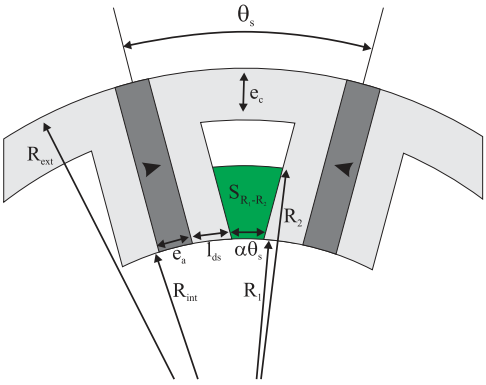

Fig. 12. Elementary cell of PM-FS or HE-FS with inner DC windings

and

$$NI_{cc_{PM}} \propto \delta_{cc_{PM}}.S_{ind_{PM}} \tag{3}$$

with B_r the magnet remanence ($1.2T$) and $h_{a_{PM}}$ the height of the magnet ($h_{a_{PM}} = R_{ext_{PM}} - R_{int_{PM}}$). Saturation effect is neglected here. $S_{ind_{PM}}$ refers to the area dedicated to the armature windings in the PM-FS machine.

2) Hybrid-Excited Flux-Switching Machine with inner DC windings

Similarly, the maximum output power of a HE-FS Flux-Switching machine $P_{max_{HE}}$ can be expressed as a function of two terms, $NI_{cc_{HE}}$ the short-circuit magnetomotive force and $\Phi_{exc_{HE}}$ the no-load flux-linkage,

$$P_{max_{HE}} \propto NI_{cc_{HE}}.\Phi_{exc_{HE}} \tag{4}$$

with

$$\Phi_{exc_{HE}} \propto B_r.h_{a_{HE}} \tag{5}$$

and

$$NI_{cc_{HE}} \propto \delta_{cc_{HE}}.S_{ind_{HE}}.\left(\frac{\Phi_{exc_{HE}}}{\Phi_{exc_{PM}}}\right) \tag{6}$$

As can be seen, value of $NI_{cc_{HE}}$ is modulated accordingly to the ratio of no-load flux-linkages $\Phi_{exc_{HE}}/\Phi_{exc_{PM}}$. $S_{ind_{HE}}$ refers to the area dedicated to the armature windings in the HE-FS machine.

In Fig. 12, a slot is depicted and the general expression of area bounded by radii R_1 and R_2 (in green) can be found as

$$S_{R_1-R_2} = \frac{\pi\left(R_2^2 - R_1^2\right)}{N_s} - \frac{R_2}{4}\left(l_{ds}\sqrt{4 - \left(\frac{\left(\frac{e_a}{2} + l_{ds}\right)}{R_2}\right)^2} + 4R_2 \arcsin\left(\frac{\left(\frac{e_a}{2} + l_{ds}\right)}{2R_2}\right)\right) + \frac{R_1}{4}\left(l_{ds}\sqrt{4 - \left(\frac{\left(\frac{e_a}{2} + l_{ds}\right)}{R_1}\right)^2} + 4R_1 \arcsin\left(\frac{\left(\frac{e_a}{2} + l_{ds}\right)}{2R_1}\right)\right) \tag{7}$$

This last expression will be helpfull to determine $S_{ind_{PM}}$ and $S_{ind_{HE}}$. Joule losses in both structures can be expressed as follows,

$$P_{J_{PM}} \propto S_{ind_{PM}}\delta_{cc_{PM}}^2 \tag{8}$$

for the PM-FS machine, and

$$P_{J_{HE}} \propto S_{ind_{HE}}\delta_{cc_{HE}}^2 \tag{9}$$

for the HE-FS machine.

B. Comparative study of PM-FSM and HE-FSM with inner DC windings

According to the foregoing model, an analysis of the influence of hybridization is provided in this section. We define an hybridization coefficient ς_{hyb} as the ratio between slot area dedicated to armature winding in both structures,

$$\varsigma_{hyb} = \frac{S_{ind_{HE}}}{S_{ind_{PM}}} \tag{10}$$

For illustrative purpose, a coefficient ς_{hyb} of 0.3 means that 70% of the initial slot area is allocated to the DC winding. Some geometrical parameters are fixed to ease the analysis. According to [18], the optimal stator slot opening $\alpha\theta_s$ of a PM-FS machine should be equal to the teeth width l_{ds},

$$l_{ds} = R_{int}\alpha\theta_s \tag{11}$$

Indeed, even if the slot area is increased reducing the tooth width, the teeth would become more heavily saturated. That may reduce the no-load flux-linkage and hence the maximal output power. On the contrary, increasing the stator tooth width to reduce the slot area should also reduce the output power for a fixed copper loss. Finally, we will consider that the permanent magnet width e_a and the external stator yoke width are both equal l_{ds}.

1) External diameter fixed

We first consider that the external diameter is fixed. Basically, in this case, just the slot area allocated to the DC excitation winding can be modified, as depicted in Fig. 13.

The influence of the hybridization coefficient ς_{hyb} on the normalized output power is presented in Fig. 14. Armature Joule losses are fixed. When the hybridization coefficient ς_{hyb} increases, the normalized output power approaches unity.

Another study is proposed in Fig. 15. The evolution of normalized armature winding Joule losses as function of the hybridization coefficient ς_{hyb} is depicted, with the ratio $P_{J_{HE}}/P_{J_{PM}}$ constant (equals to 1). As can be seen, when the ratio ς_{hyb} decreases, armature Joule losses dramatically increase. For instance, when $\varsigma_{hyb} = 0.5$, Joule losses are twice greater.

2) External diameter variable

Now to determine influence of the hybridization coefficient ς_{hyb} on volume requirement, the external diameter is not fixed anymore. In Fig. 16, the modification allowed in this paragraph is depicted.

In Fig. 17, the evolution of ratio $P_{J_{HE}}/P_{J_{PM}}$ as function of ratio $R_{ext_{HE}}/R_{ext_{PM}}$, considering the output power constant

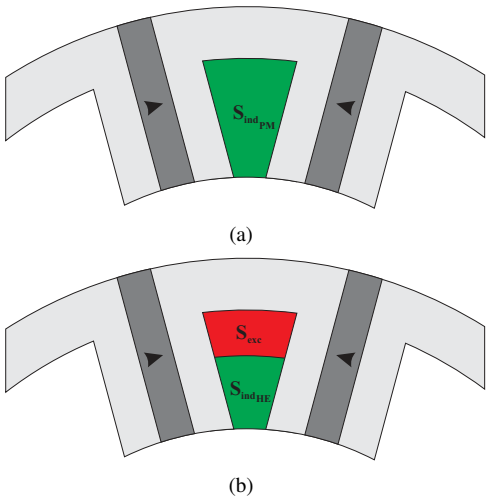

Fig. 13. Elementary cell with fixed external diameter: initial structure PM-FS machine (a) and HE-FS machine with inner DC windings (b)

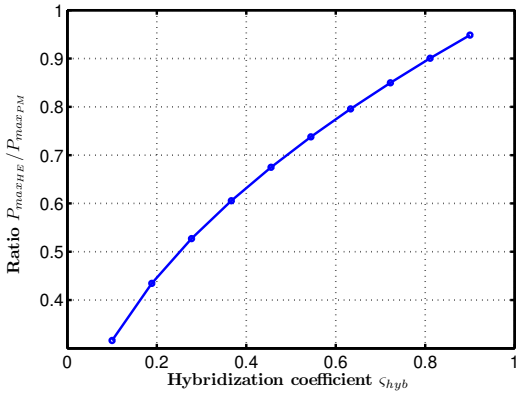

Fig. 14. Evolution of the normalized output power $P_{max_{HE}}/P_{max_{PM}}$ as function of hybridization coefficient ς_{hyb} for fixed armature winding Joule losses

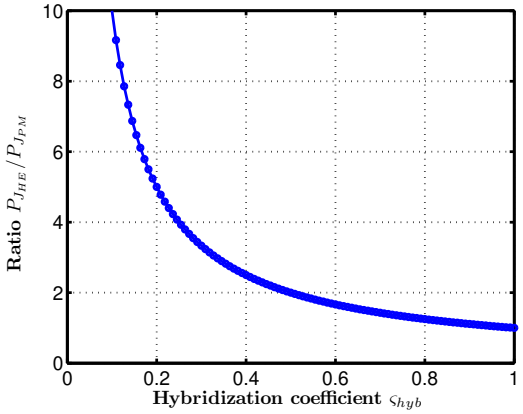

Fig. 15. Evolution of the normalized armature winding Joule losses $P_{max_{HE}}/P_{max_{PM}}$ as function of hybridization coefficient ς_{hyb} for fixed output power ($P_{max_{HE}}/P_{max_{PM}} = 1$)

($P_{max_{HE}}/P_{max_{PM}} = 1$) and for different values of the hybridization coefficient ς_{hyb}, is proposed.

Intersections between iso-power curves and the constant

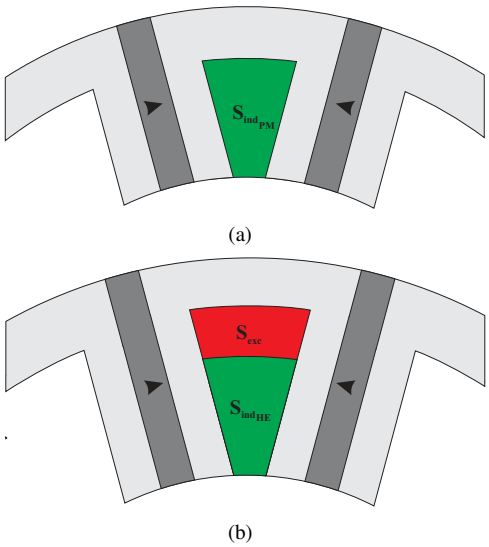

Fig. 16. Elementary cell with variable external diameter: initial structure PM-FS machine (a) and HE-FS machine with inner DC windings (b)

curve ($P_{J_{HE}}/P_{J_{PM}} = 1$) allow ones to determine the increase of volume to meet Joule losses and output power requirements. By way of example, considering a hybridization coefficient $\varsigma_{hyb} = 0.7$, the external radius R_{ext_h} should increase by 5% (internal radius $R_{ext_{HE}} = R_{ext_{PM}}$ is kept constant here).

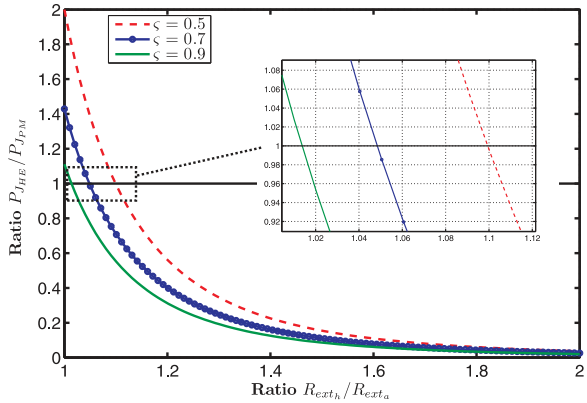

Fig. 17. Evolution of the normalized armature winding Joule losses $P_{max_{HE}}/P_{max_{PM}}$ as function of ratio $R_{ext_{HE}}/R_{ext_{PM}}$ for fixed output power ($P_{max_{HE}}/P_{max_{PM}} = 1$) and different hybridization coefficients ς_{hyb}

VI. Serie or parallel flux-path HE-FS Machine ?

As explained in the introduction, Hybrid Excited Machines mainly can be sorted into two groups: series or parallels flux-paths machines. In this section, we will try to determine in which group this HE-FS topology falls into. We will first investigate the influence of combination of stator and rotor pole number. In Fig. 18.(a) is depicted the evolution of the peak flux-linkage φ_{max} for a LL-DCw topology having 12 stator poles and 10 or 14 rotor teeth. As shown before, only flux-weakening operation can be achieved. The maximum flux-linkage (for $\delta_{exc} = 0A.mm^{-2}$) obtained with 2D FE analysis is higher for the 10-teeth rotor ($\varphi_{max} = 460\mu Wb$) than for the 14-teeth rotor ($\varphi_{max} = 410\mu Wb$).

It is shown that in both cases the phase flux-linkage can be easily tuned. However, the structure having 14 rotor teeth has a higher flux weakening operation (Figs. 18.(b) and (c)). Indeed, if we consider a DC excitation current density of $10A.mm^{-2}$, the phase flux-weakening ratio ξ is about 3 for the 10 rotor teeth structure while ξ equals 10 for the 14 teeth structure. Thus, taking note of this finding, we can conclude that the effectiveness of the DC winding has a close relationship with the number of rotor teeth. It also means that the DC winding permeance has a lower value when the rotor has 10 teeth than 14 teeth.

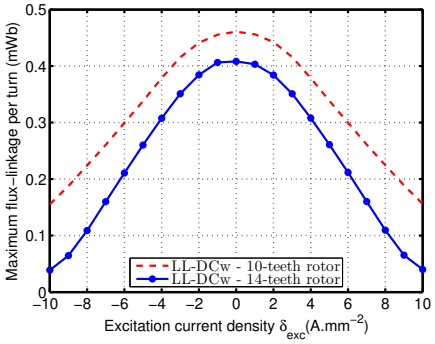

(a)

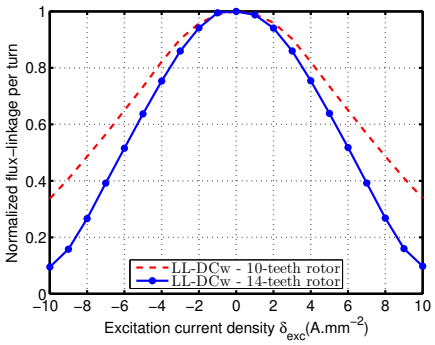

(b)

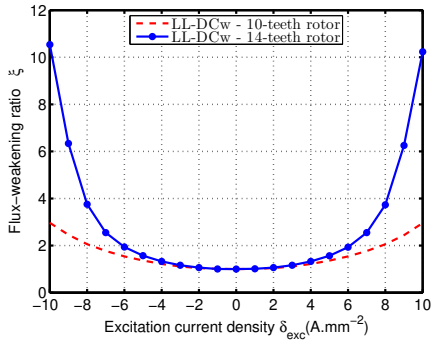

(c)

Fig. 18. Maximum flux-linkage per turn (a), normalized flux-linkage per turn (b) and flux-weakening ratio ξ (c) as function of DC excitation current density δ_{exc} and for different rotor teeth number)

To corroborate this assumption, we explored, through FE analysis, the flux lines created by the DC winding (as the only source) for different rotor teeth number. In Fig. 19 are presented the equipotential lines of the magnetic vector

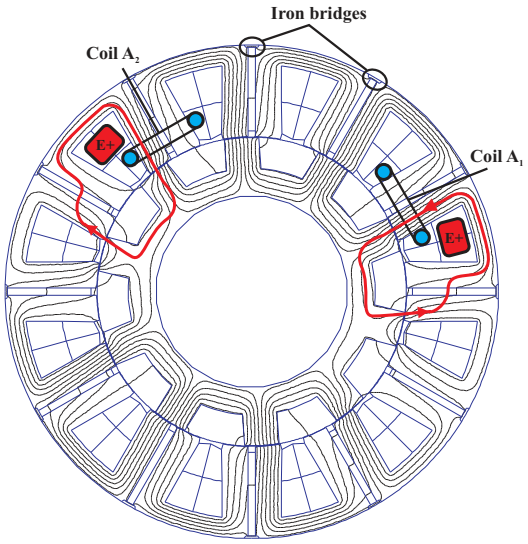

(a)

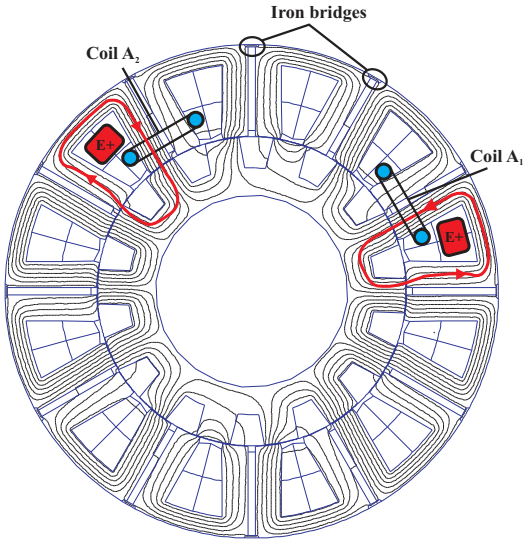

(b)

Fig. 19. Flux lines created by the DC excitation winding when the rotor in at the d-axis position and PMs are replaced by air for a 12 stator poles configuration: 10 rotor teeth (a) and 14 rotor teeth (b)

potential, respectively for 10 and 14 rotor teeth configurations. PMs are replaced by air and we still consider that U-shaped stator cores are both linked with a thin iron bridge (1mm thickness).

As can be seen, the main flux path of DC windings are depicted in red lines. In the case of the 10-teeth rotor (See Fig. 19.(a)), the reluctance of the DC winding, $\Re_{DCw}$, is higher than the 14-teeth rotor. Indeed, the main flux has to flow through the magnet (Fig. 19.(a)) which has a magnetic permeability μ very low, close to that of air. On the contrary, with the 14-teeth rotor, the DC winding flux can directly loop back through the stator core (Fig. 19.(b)) without additional air-gap because of its narrowest rotor pole pitch.

Finally, to conclude this point, this HE-FS machine having inner DC windings belongs to both types of hybrid-excited machines depending on the stator rotor teeth combination chosen: series flux-paths machine with the 10-teeth rotor or

parallels flux-paths machine with the 14-teeth rotor. However, the 14-teeth rotor configuration exhibits a higher back-emf and also a greater flux-weakening capability.

VII. Experimental validation of working principle

In this section, an experimental validation is proposed. First, we detail some key points in the design of the structure.

A. Design considerations

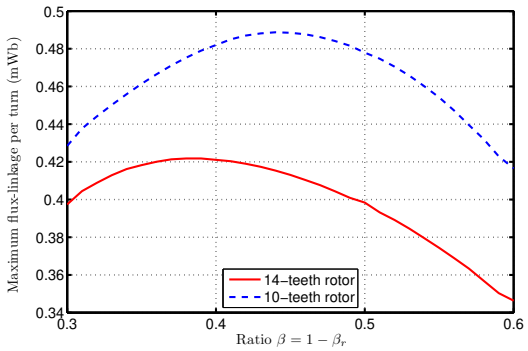

(a)

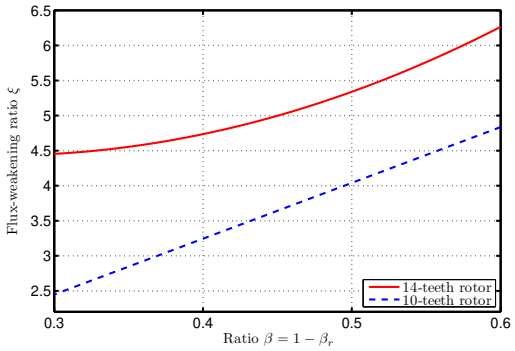

(b)

Fig. 20. Evolution of maximum flux-linkage (a) and flux-weakening ratio ξ (b) as function of the relative rotor tooth opening β

The design was based on a parametric optimization, notably the rotor teeth width, which is particularly important. In Fig. 20.(a), the evolution of the maximum flux-linkage as function of the relative rotor tooth opening β, for both rotor configurations. As can be seen, the maximum flux-linkage is achieved for $beta = 0.44$ for the 10-teeth rotor, and $\beta = 0.39$ for the 14-teeth rotor. The flux-linkage is always higher with the 10-teeth than with the 14-teeth rotor. The evolution of the flux-weakening ratio ξ as function of β is proposed in Fig. 20.(b). As expected, the 14-teeth rotor allows controlling more efficiently the phase flux-linkage than the 10-teeth rotor. Indeed, the flux-weakening ratio ξ equals 3.5 for $\beta = 0.44$ with the 10-teeth rotor, while it reaches 4.7 with the 14-teeth rotor ($\beta = 0.39$).

Regarding the stator teeth opening, as suggested in [18], we took it equal to the stator slot opening.

(a)

(b) (c)

Fig. 21. Prototype machine of the HE-FSM with inner DC windings: 12 stator slots (a), 10-teeth rotor (b) and 14-teeth rotor (c)

B. Experimental validation

To validate the foregoing 2D FE analysis, a prototype machine having 12 stator slots was manufactured (Figs. 21.(a), (b) and (c)). The main idea was to demonstrate the working principle of this new topology through an experimental proof-of-principle. Also, we highlighted in previous sections that the stator and rotor teeth combinations could be directly related to DC winding effectiveness. Therefore, we realized two different rotors with respectively 10 and 14 teeth. Major design parameters of the prototype are summarized in Table I. For both rotor, *i.e.* 10 and 14 teeth rotors, the rotor pole width equals half of rotor pole pitch.

Electromagnetic performances at no-load of the prototype machines (for each rotor) were predicted by 2D FE analysis and compared with measured results. As shown in Fig. 22, the RMS value of back-emf can be easily adjusted with the DC excitation current, validating previous findings, notably the operation principle.

Although the 2D FE predicted back-emfs are higher (difference between $5-8V$ for the 14-teeth rotor and between $4-6V$ for the 10-teeth rotor) than the measured results due to the end effect, fair agreement is achieved. In particular, trends of variation of back-emf with DC excitation current are in fair agreement with measurements for both rotor configurations.

Also, experimental results show that the 14-teeth rotor machine exhibits a larger field-weakening capability ($\xi = 20$ experimentally) than that of the 10-rotor pole machine ($\xi = 7.8$ by experiments).

	HE-FSM with inner DC windings	
Number of phases q	3	
Number of stator poles N_s	12	
Number of rotor teeth N_r	10	14
Stator outer radius (mm)	90	
Active length (mm)	30	
Air-gap length (mm)	0.3	
Rotor outer radius (mm)	56.2	
PM thickness (mm)	2.6	
Rotor teeth width (mm)	18	12.6
Magnet remanence (T)	1.15	
Number of turns of DC excitation windings per coils	85	
Number of turns per coils	60	

TABLE I
MAJOR DESIGN PARAMETERS OF HE-FSM WITH INNER DC WINDINGS

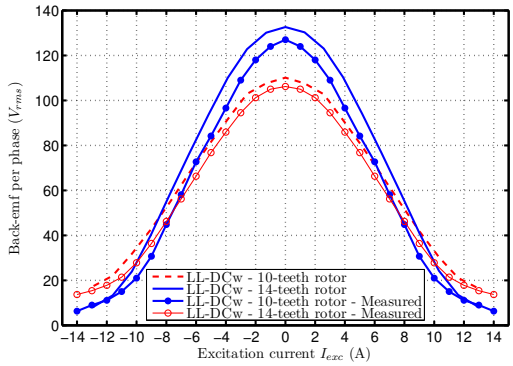

Fig. 22. Evolution of back-emf as function of DC excitation current I_{exc} - LL-DCw configuration with 10- and 14-teeth rotor - Comparison between measurements and 2D FE simulations - $N = 1500rpm$

VIII. HIGH-SPEED OPERATION OF THE HE-FS DC-ALTERNATOR

As stated in the introduction, we want to demonstrate that the HE-FS proposed here is suitable for high speed, notably regarding the thermal limitation. In so doing, the prototype machine was tested as a DC-Alternator [19][20] under a wide range of speeds, up to 12000rpm. It is worth mentioning that according to its working principle, the maximum output power is achieved for $I_{exc} = 0A$. This means that no additional Joule losses comes to degrade the thermal performances. This is not the case for others HE-FS machines presented in the introduction. Actually, contrary to the proposed machine, the existing topologies need additionnal excitation magnetomotive force to achieve the maximum phase flux-linkage or output torque, creating additional Joule losses (See Section II).

A. Experimental set-up description

The DC-bus voltage (Diode Bridge Rectifier -DBR - output voltage) is considered as constant and the power converter (association of HE-FS Machine and DBR) can be assimilated to a current rectifier (each diode conducts 180 electrical degree). The scheme of the experimental set-up is given in Fig. 23. An induction motor of 5.5 kW is employed as prime mover of the HEFSPM Generator and powered by a three-phase inverter. The DBR is connected on the same DC-bus voltage feeding the 3-phase inverter controlling the induction motor. Hence, the grid is just providing the losses of the overall system: mainly mechanical losses due to the chain drive. Indeed, it should be mentioned that the AC/DC converter connected between the grid and the DC-bus is a Diode Bridge Rectifier too, so has an unidirectional power flow.

The DC winding current is manually controlled using an additional external DC voltage source.

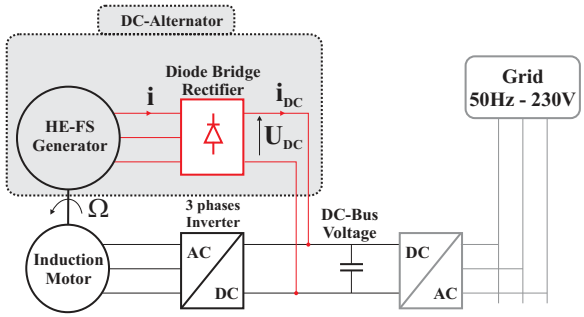

Fig. 23. Scheme of the experimental set-up

B. Thermal analysis based on experiments

As can be seen in Fig. 24, the DC output power of the machine rapidly (2000 rpm after the base speed) set up to a maximum (normalized output power) as the speed increases. Indeed, the diode bridge rectifier imposes that the fundamental of phase-neutral voltage is in phase with the fundamental of the line current. This point is validated experimentally in Fig. 25, where waveforms of phase voltage (pink line), phase current (light blue) and the DC output current (dark blue) are depicted. Those waveforms were captured for a rotating speed of 12000rpm.

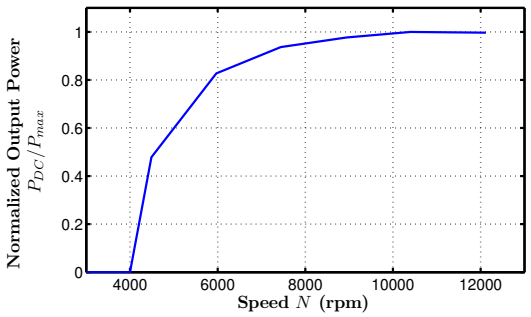

Fig. 24. Evolution of DC output power as function of speed

It was also possible to assess the efficiency experimentally using a lever arm to determine the mechanical torque. Then, the losses occuring in the machine were obtained substracting the DC output power from the mechanical losses. In Fig. 26, the evolution of efficiency as function of speed are superimposed.

For low speeds, *i.e.* under 7000rpm, the efficiency stays over acceptable level (80%). However, over that speed, efficiency dramatically decreases due to additionnal mechanical losses and iron losses. As can be seen, for a rotating speed of 12000

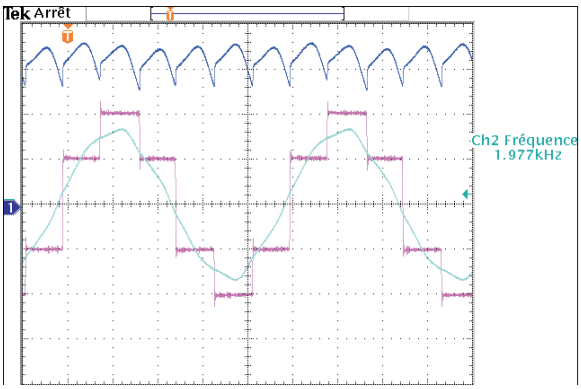

Fig. 25. Captured waveforms of phase voltage (pink line), phase current (light blue) and DC output current (dark blue) at 12000 rpm

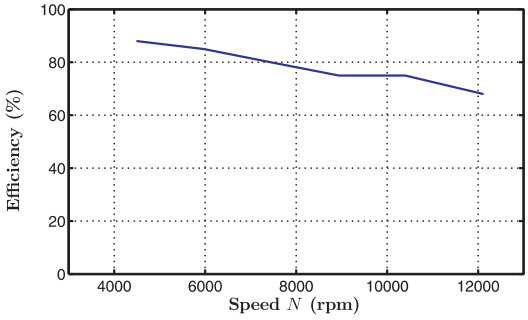

Fig. 26. Evolution of efficiency as function of speed

rpm, losses reach a maximum, and so, the thermal constraint is the highest. For this highest-contrained operating point, we determine if a thermal stabilization is achieved. Using a thermal camera (Fluke TI 20), the evolution of the temperature was captured as shown in Fig. 27, especially for the active parts as phase windings. It is found that the temperature after 1 hour of tests stabilizes around $56°C$ for phase windings and $48°C$ for DC windings (the hotspot around $108°C$ in Fig. 27 is due to reflexion of rotor and should not be considered). Hence, the prototype is suitable for high speed operation. We could not perform experiments under higher speed because of the prime mover speed limitation.

C. 2D Finite-Element thermal model

A thermal model is developed to propose a qualitative analysis of the thermal behavior of the structure. Some assumptions are made to develop the 2D FE thermal model of the HE-FS machine with inner DC windings.

First, the air-gap is doubly salient, thus, we can consider that we are in a turbulent flow regime. Thus, we can assume that the air at the middle of air-gap is isothermal. This means that losses in the rotor are dissipated axially. On the contrary, heat transfer in the stator will be purely radial. This assuption has been made in [21][22] and was validated experimentally.

Hence, based on the foregoing assumptions, a simplified geometry for the thermal simulation can be proposed. In Fig. 28, the equivalent model is depicted with the associated boundary conditions.

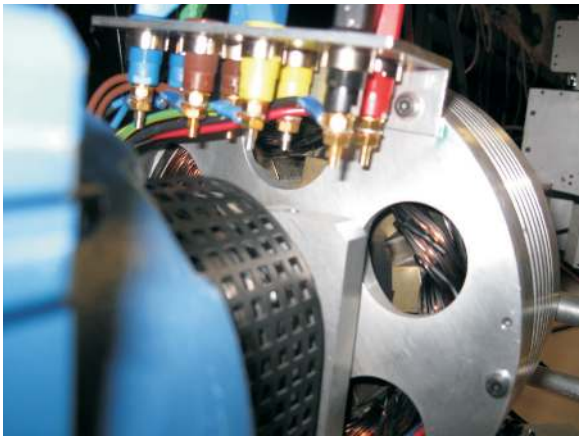

(a)

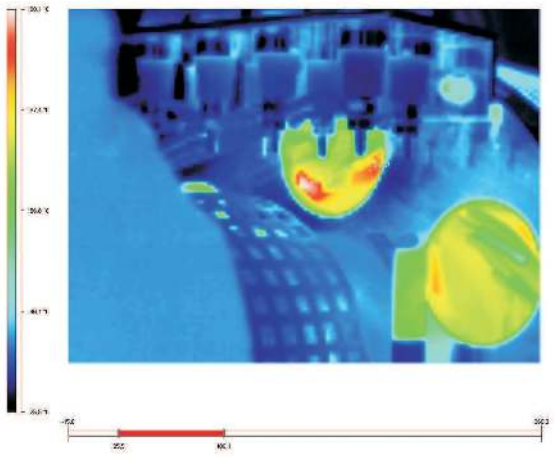

(b)

Fig. 27. Prototype machine (a) and thermal image captured at 12000 rpm (b)

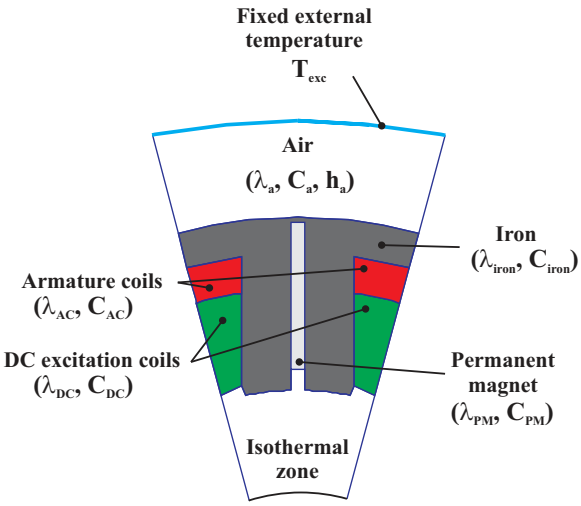

Fig. 28. Considered geometry for the thermal 2D FE simulation

Each zone of the stator is defined by their own thermal conductivity λ and also their volumetric heat capacity C. Also, the air surrounding the stator is defined by a convective heat-transfer coefficient h_a.

We consider that heat sources in the stator are both Joule

	Conductivity $(W/m/°C)$	Specific heat capability $(J/kg/°C)$	Heat transfer coefficient $(W/m^2/°C)$
Air	0.03	1005	30
Iron	30	460	0
PM	16.5	440	0
Equivalent windings	0.8469	482.7	0

TABLE II
THERMAL DATA FOR 2D FE SIMULATIONS

losses in coils and also iron losses in the stator. Evaluation of iron losses is based on efficiency determined experimentally (See Fig. 26). In flux-switching machines, stator iron losses represents around 70% of total iron losses. Also, we assume that the heat generation is homogeneous on each zone (iron or windings). In [23], authors took the same assumptions to model. Thermal data is summarized in Table VIII-C.

FE results presented in Fig. 29 show a temperature rise around $60°C$ which is consistent with experiments.

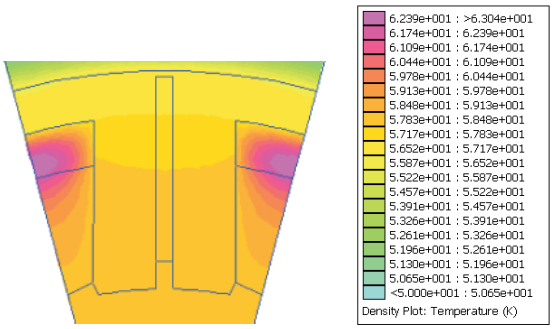

Fig. 29. Thermal 2D FE simulation at $12000rpm$ and for the maximum output power P_{max} (No DC current)

D. Thermal analysis under flux-weakening mode

We finally evaluate the influence of flux-weakening mode on the thermal behavior of the proposed HE-FS machine with inner DC windings. In so doing, we performed another experiment at $12000rpm$, still in DC-alternator mode. We cannot rotate above this speed because of limitation of the prime mover (an induction motor). We increased the DC current, so that the maximum output power P_{max} (achieved without DC field) is divided by two.

In Fig. 30, 2D FE thermal results in flux-weakening mode are proposed, and should be compared to those presented in Fig. 29 without DC current. In flux-weakening mode, temperature is maximum in the excitation slot region. It should be noted that teperature rises to $90-100°C$ with a DC current of $5A$.

Experiments performed at the same speed and the same excitation current are in fair accordance with $82°C$ for phase windings and $100°C$ for excitation windings. Also, it should be noted that in flux-weakening mode, because of additionnal excitation Joule losses, the thermal constraint is more important. As can be seen, in Fig. 30, the stator iron is also heated up. Both simulations and experiments emphasize this phenomenon, with a rise of temperature around $40°C$ which is still acceptable.

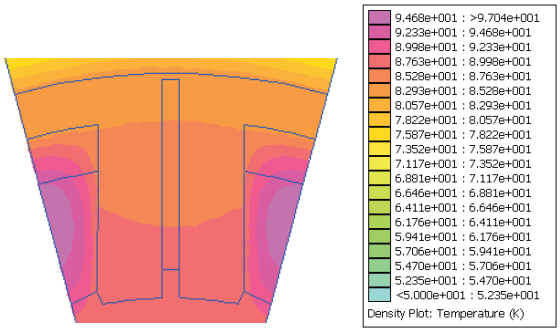

Fig. 30. Thermal 2D FE simulation at $12000rpm$ in flux-weakening operation $P_{max}/2$: Excitation current $I_{exc} = 5A$

IX. CONCLUSION

In this paper, a novel hybrid excited flux-switching machine is proposed and its operation principle presented. This topology has all excitation sources located on the stator. Based on FE analysis, simulation results predict good field control. Thus, this structure could be really interesting for variable-speed applications. Indeed, the maximum output power is achieved without DC current improving efficiency and the thermal behavior.

We explored and demonstrated that the flux-weakening operation is achieved thanks to the DC winding that acts differently on each coil of the same phase and introduce notably an homopolar component. However, it was shown that the total phase flux-linkage keeps a sinusoidal-like waveform, even during flux-weakening operation.

The proposed HE-FS topology with inner DC windings reduces the area which can be used for main phase windings. As a direct consequence it would impact on the efficiency and volume requirement of the machine. This point is addressed by means of a theoretical approach, which is by-turn based on power equations.

Also, the influence of stator pole - rotor teeth number combination was investigated. Indeed, we found that it directly impacts on the efficiency of the flux-linkage control. The DC winding permeance being higher with a 14 teeth rotor, this topology could be classified as a parallels flux-paths HE-FSM. On the contrary, the 10 rotor teeth topology belongs to series flux-paths HE-FSM.

A prototype was built to corroborate FE simulations and confirm the working principle. Two rotors were built also, with 10 or 14 teeth, to validate the foregoing analysis. The prototype machine showed, during experimentations, an excellent control of the back-emf. Also, 2D FE predicted performances were experimentally validated with an acceptable accuracy and good trends of variation.

Finally, a set of experiments were led on-load (DC Alternator operation). Results show clearly that this novel Hybrid-Excited Flux-Switching machine is suitable for high speed operation. Regarding the thermal behavior, it was shown that the temperature does not exceed $60°C$ at 12000rpm and for

the maximum output power. These good performances have to be related to the working principle of this topology that does not require additionnal excitation magnetomotive force to reach the maximum output power.

An extented thermal analysis in flux-weakening mode was also proposed. We showed that the thermal constraint increases because of additionnal Joule losses. However, thermal elevation stays under acceptable levels.

REFERENCES

[1] A. El-Refaie, "Fractional-slot concentrated-windings synchronous permanent magnet machines: Opportunities and challenges," *IEEE Trans. Ind. Electron.*, vol. 57, no. 1, pp. 107 –121, jan. 2010.

[2] Z. Sun, J. Wang, G. Jewell, and D. Howe, "Enhanced optimal torque control of fault-tolerant pm machine under flux-weakening operation," *IEEE Trans. Ind. Electron.*, vol. 57, no. 1, pp. 344 –353, jan. 2010.

[3] Y. Amara, L. Vido, M. Gabsi, E. Hoang, A. Hamid Ben Ahmed, and M. Lecrivain, "Hybrid excitation synchronous machines: Energy-efficient solution for vehicles propulsion," *IEEE Trans. Veh. Technol.*, vol. 58, no. 5, pp. 2137 –2149, jun 2009.

[4] A. Ibala and A. Masmoudi, "Accounting for the armature magnetic reaction and saturation effects in the reluctance model of a new concept of claw-pole alternator," *IEEE Trans. Magn.*, vol. 46, no. 11, pp. 3955 –3961, nov. 2010.

[5] J. Tapia, F. Leonardi, and T. Lipo, "Consequent-pole permanent-magnet machine with extended field-weakening capability," *IEEE Trans. Ind. Appl.*, vol. 39, no. 6, pp. 1704 – 1709, nov.-dec. 2003.

[6] S.-U. Chung, J.-W. Kim, B.-C. Woo, D.-K. Hong, J.-Y. Lee, and D.-H. Koo, "A novel design of modular three-phase permanent magnet vernier machine with consequent pole rotor," *IEEE Trans. Magn.*, vol. 47, no. 10, pp. 4215 –4218, oct. 2011.

[7] R. Owen, Z. Zhu, and G. Jewell, "Hybrid-excited flux-switching permanent-magnet machines with iron flux bridges," *IEEE Trans. Magn.*, vol. 46, no. 6, pp. 1726 –1729, june 2010.

[8] Y. Wang and Z. Deng, "Hybrid excitation topologies and control strategies of stator permanent magnet machines for dc power system," *Industrial Electronics, IEEE Transactions on*, vol. 59, no. 12, pp. 4601–4616, 2012.

[9] A. Zulu, B. Mecrow, and M. Armstrong, "Investigation of the dq-equivalent model for performance prediction of flux-switching synchronous motors with segmented-rotors," *IEEE Trans. Ind. Electron.*, vol. PP, no. 99, p. 1, 2011.

[10] W. Zhao, M. Cheng, K. Chau, R. Cao, and J. Ji, "Remedial injected-harmonic-current operation of redundant flux-switching permanent-magnet motor drives," *IEEE Trans. Ind. Electron.*, vol. 60, no. 1, pp. 151 –159, jan. 2013.

[11] T. Raminosoa, C. Gerada, and M. Galea, "Design considerations for a fault-tolerant flux-switching permanent-magnet machine," *IEEE Trans. Ind. Electron.*, vol. 58, no. 7, pp. 2818 –2825, july 2011.

[12] W. Zhao, M. Cheng, W. Hua, H. Jia, and R. Cao, "Back-emf harmonic analysis and fault-tolerant control of flux-switching permanent-magnet machine with redundancy," *IEEE Trans. Ind. Electron.*, vol. 58, no. 5, pp. 1926 –1935, may 2011.

[13] W. Hua, M. Cheng, and G. Zhang, "A novel hybrid excitation flux-switching motor for hybrid vehicles," *IEEE Trans. Magn.*, vol. 45, no. 10, pp. 4728 –4731, oct. 2009.

[14] E. Hoang, M. Lecrivain, and M. Gabsi, "A new structure of a switching flux synchronous polyphased machine with hybrid excitation," in *Power Electronics and Applications, 2007 European Conference on*, sept. 2007, pp. 1 –8.

[15] J. Chen, Z. Zhu, S. Iwasaki, and R. Deodhar, "A novel hybrid excited flux-switching brushless ac machines for ev/hev applications," in *Vehicle Power and Propulsion Conference (VPPC), 2010 IEEE*, sept. 2010, pp. 1 –6.

[16] E. Hoang, M. Lecrivain, and M. Gabsi, "Flux-switching dual excitation electrical machine," Patent PCT/EP2007/052 167, 2007.

[17] M. Cheng, W. Hua, J. Zhang, and W. Zhao, "Overview of stator-permanent magnet brushless machines," *IEEE Trans. Ind. Electron.*, vol. 58, no. 11, pp. 5087 –5101, nov. 2011.

[18] Z. Zhu, Y. Pang, D. Howe, S. Iwasaki, R. Deodhar, and A. Pride, "Analysis of electromagnetic performance of flux-switching permanent-magnet machines by nonlinear adaptive lumped parameter magnetic circuit model," *IEEE Trans. Magn.*, vol. 41, no. 11, pp. 4277 – 4287, nov. 2005.

[19] Z. Zhang, Y. Tao, and Y. Yan, "Investigation of a new topology of hybrid excitation doubly salient brushless dc generator," *IEEE Trans. Ind. Electron.*, vol. 59, no. 6, pp. 2550 –2556, june 2012.

[20] Y. Wang and Z. Deng, "Hybrid excitation topologies and control strategies of stator permanent magnet machines for dc power system," *IEEE Trans. Ind. Electron.*, vol. 59, no. 12, pp. 4601 –4616, dec. 2012.

[21] G. Li, J. Ojeda, E. Hoang, M. Lecrivain, and M. Gabsi, "Comparative studies between classical and mutually coupled switched reluctance motors using thermal-electromagnetic analysis for driving cycles," *Magnetics, IEEE Transactions on*, vol. 47, no. 4, pp. 839–847, 2011.

[22] J. Ojeda, M. Simoes, G. Li, and M. Gabsi, "Design of a flux-switching electrical generator for wind turbine systems," *Industry Applications, IEEE Transactions on*, vol. 48, no. 6, pp. 1808–1816, 2012.

[23] J.-F. Trigeol, Y. Bertin, and P. Lagonotte, "Thermal modeling of an induction machine through the association of two numerical approaches," *Energy Conversion, IEEE Transactions on*, vol. 21, no. 2, pp. 314–323, 2006.

Gaussens Benjamin (S'11) was born in Toulouse, France, in 1987. He received the M.Sc. degree in electrical engineering from the Institut National Polytechnique (ENSEEIHT), Toulouse, France. He is currently working toward the Ph.D. degree still in electrical engineering at SATIE, ENS Cachan, CNRS, UniverSud. His current research interests include design of innovative topology of electromagnetic actuators and their modeling.

Hoang Emmanuel was born in Antibes, France, in 1966. He received the "agrégation" in electrical engineering in 1990 and the Ph.D. degree from the Ecole Normale Supérieure de Cachan in 1995. Since 1990, he has worked with the electrical machine team in the SATIE laboratory. His research interests include the modeling of the iron losses in SRMs and the design, modeling, optimization, and control of novel topologies of PM machines.

Lécrivain Michel was born in Barneville, France. He received the degree in electrical engineering from the Conservatoire National des Arts et Métiers (CNAM, Paris, France) in 1981. In 1997 he joined SATIE laboratory as a Research Engineer. His research interests include the design and control of new hybrid machines and novel permanent-magnet machines for automotive applications.

Manfe Philippe was born in 1955. He received the degree in engineering from Ecole Nationale Supérieure d'Electricité et de Mécanique, and the Ph.D. degree from the Institut National Polytechnique de Lorraine, Nancy, France. From 1981 to 1984, he was with the French National Scientific Research Center (CNRS). In 1985, he joined Leroy Somer Motors and Drive Division, Angoulême, France to Design and Develop high performance motors and drives for industrial and automotive markets. In 1997 he joined the Alternators Division as Electrical Engineering Manager, and is currently Engineering Director for LV Generators in Emerson/LS Electric Power Generation Division.

Gabsi Mohamed (M'93) received the Ph.D. degree in electrical engineering from University of Paris-VI in 1987 and the HDR in 1999 from University of Paris-XI (Orsay, France). Since 1990, he has been working with the electrical machine team (SETE, Systèmes d'Energies pour le Transport et l'Environnement) of SATIE laboratory where he is currently a Full Professor and the Director of the Electrical Engineering Department. His research interests include SRM, vibrations and acoustic noise, and PM machines.